ADVANCED MATERIALS
www.advmat.de

# Reversibly Controlled Ternary Polar States and Ferroelectric Bias Promoted by Boosting Square-Tensile-Strain

*Jun Han Lee, Nguyen Xuan Duong, Min-Hyoung Jung, Hyun-Jae Lee, Ahyoung Kim, Youngki Yeo, Junhyung Kim, Gye-Hyeon Kim, Byeong-Gwan Cho, Jaegyu Kim, Furqan Ul Hassan Naqvi, Jong-Seong Bae, Jeehoon Kim, Chang Won Ahn, Young-Min Kim, Tae Kwon Song, Jae-Hyeon Ko, Tae-Yeong Koo, Changhee Sohn, Kibog Park, Chan-Ho Yang, Sang Mo Yang, Jun Hee Lee, Hu Young Jeong, Tae Heon Kim,* and Yoon Seok Oh**

**Interaction between dipoles often emerges intriguing physical phenomena, such as exchange bias in the magnetic heterostructures and magnetoelectric effect in multiferroics, which lead to advances in multifunctional heterostructures. However, the defect-dipole tends to be considered the undesired to deteriorate the electronic functionality. Here, deterministic switching between the ferroelectric and the pinched states by exploiting a new substrate of cubic perovskite, $BaZrO_3$ is reported, which boosts the square-tensile-strain to $BaTiO_3$ and promotes four-variants in-plane spontaneous polarization with oxygen vacancy creation. First-principles calculations propose a complex of an oxygen vacancy and two $Ti^{3+}$ ions coins a charge-neutral defect-dipole. Cooperative control of the defect-dipole and the spontaneous polarization reveals ternary in-plane polar states characterized by biased/pinched hysteresis loops. Furthermore, it is experimentally demonstrated that three electrically controlled polar-ordering states lead to switchable and nonvolatile dielectric states for application of nondestructive electro-dielectric memory. This discovery opens a new route to develop functional materials via manipulating defect-dipoles and offers a novel platform to advance heteroepitaxy beyond the prevalent perovskite substrates.**

## 1. Introduction

Anisotropic interactions between order parameters have provided innovative pathways for developing functional devices on the peculiar physical properties. For example, anisotropic exchange interaction at the interface between a ferromagnetic and an antiferromagnetic layer generates exchange bias effect (**Figure 1**a), which has been a key property to realize magnetic readback heads and magnetic random access memory devices.[1,2] Antisymmetric exchange interaction, known as Dzyaloshinky–Moriya interaction, between neighboring magnetic moments builds up magnetically induced electric polarization and magnetoelectric effect in multiferroic.[3] For ferroelectrics, however, the anisotropic interactions between electric dipoles have been imitated by spatial electric potential gradient, rather than a cooperative dipolar unit element, resulting in imprint

J. H. Lee, G.-H. Kim, C. Sohn, K. Park, Y. S. Oh
Department of Physics
Ulsan National Institute of Science and Technology (UNIST)
Ulsan 44919, Republic of Korea
E-mail: ysoh@unist.ac.kr

N. X. Duong, C. W. Ahn, T. H. Kim
Department of Physics and Energy Harvest-Storage Research Center (EHSRC)
University of Ulsan
Ulsan 44610, Republic of Korea
E-mail: thkim79@ulsan.ac.kr

M.-H. Jung, Y.-M. Kim
Department of Energy Science
Sungkyunkwan University
Suwon 16419, Republic of Korea

The ORCID identification number(s) for the author(s) of this article can be found under https://doi.org/10.1002/adma.202205825.

**DOI: 10.1002/adma.202205825**

H.-J. Lee, J. H. Lee
School of Energy and Chemical Engineering
Ulsan National Institute of Science and Technology (UNIST)
Ulsan 44919, Republic of Korea

A. Kim, S. M. Yang
Department of Physics
Sogang University
Seoul 04107, Republic of Korea

Y. Yeo, J. Kim, C.-H. Yang
Department of Physics & Center for Lattice Defectronics
Korea Advanced Institute of Science and Technology (KAIST)
Daejeon 34141, Republic of Korea

J. Kim, K. Park
Department of Electrical Engineering
Ulsan National Institute of Science and Technology
Ulsan 44919, Republic of Korea

B.-G. Cho, T.-Y. Koo
Pohang Accelerator Laboratory
Pohang University of Science and Technology (POSTECH)
Pohang, Gyeongbuk 790-784, Republic of Korea

 

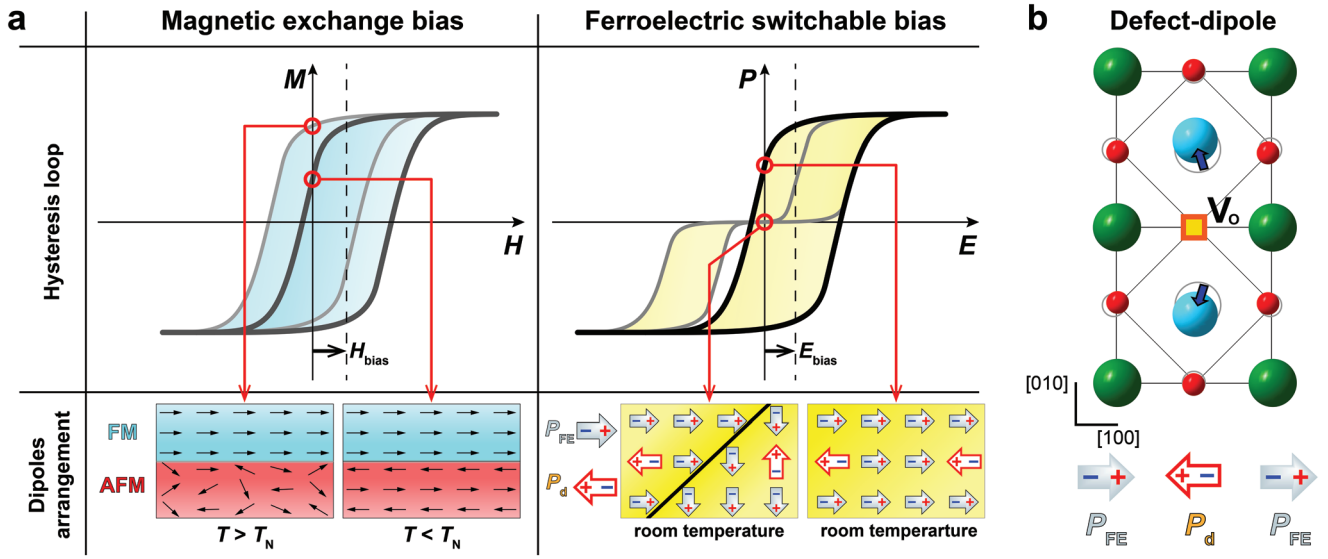


**Figure 1.** Switchable ferroelectric bias in hysteresis loop and theoretical calculations for a defect-dipole of a $Ti^{3+}$–$V_O$–$Ti^{3+}$ complex. a) Anisotropic interactions and characteristic hysteresis loops of magnetic heterostructures and ferroelectrics. Exchange interaction at an interface between ferromagnetic and antiferromagnetic layers leads to $H_{bias}$ biased hysteresis loop of the magnetic heterostructures. For ferroelectrics, defect-dipole $P_d$ in the lattice can play a role in the bias-field $E_{bias}$. Cooperation of the $P_d$, spontaneous polarization $P_{FE}$, and domain arrangement enables deterministic control of ferroelectric bias, characterized by either pinched or biased hysteresis loop. b) DFT calculations simulate local $Ti^{3+}$ and $O^{2-}$ ion displacements of 0D defect-dipole when the $P_{FE}$ is oriented along the [100]-direction and a point oxygen vacancy $V_O$ is located at a vertex of the [010]-axis in a $TiO_6$ octahedron (see the Materials and Methods in the Supporting Information). The green, blue, and red spheres represent barium ($Ba^{2+}$), trivalent titanium ($Ti^{3+}$), and oxygen ($O^{2-}$) ions, respectively. The yellow square indicates a $V_O$. The open gray circles show the ions' initial positions without the $V_O$. The dark blue arrows illustrate the $Ti^{3+}$ ion displacements from the initial positions. Two $Ti^{3+}$ ions neighboring the $V_O$ are displaced away from the $V_O$ so that the $V_O$ leads to canted displacement of the $Ti^{3+}$ ions and finite $P_d$ of the canted $Ti^{3+}$–$V_O$–$Ti^{3+}$ complex.

and voltage shift in ferroelectric hysteresis loop $P(E)$.[4–7] It has been extensively studied that the spatial electric potential gradient originates from various sources, such as charge trapping/migration/injection,[8] built-in field attributed to a difference in the work function between the asymmetric top and bottom electrodes,[9] strain-gradient-induced flexoelectric field,[10] surface polar absorbates,[11] and interfacial Schottky effect.[12] Such spatial potential gradient easily appears in the vertical geometry of ferroelectric heterostructures and provokes the instability (e.g., polarization fatigue/relaxation, retention loss, depolarization, and self-polarization) of switchable polarization.[13] Furthermore, the congenital slow dynamics or stationary property circumscribe versatile application and technological advances in functionality of the nonvolatile ferroelectric memory devices.

For ferroelectric properties, the noncentric charge distribution of the oxygen vacancy $V_O$ produces a defect-dipole $P_d$, which has been known to deteriorate ferroelectricity or to enhance piezoelectricity.[14] Here, we take advantage of anisotropic interaction between $P_d$ and spontaneous polarization $P_{FE}$, and demonstrate to reversibly manipulate the direction of internal bias-field $E_{bias}$ in the ferroelectric hysteresis loop similar to the exchange bias effect in magnetic heterostructures (Figure 1a).[1,2] In order to prohibit the spatially asymmetric electric potential gradient and construct isotropic geometry of a device, we design in-plane polarized ferroelectric heterostructures within the horizontal geometry by applying square tensile stress in the (001) plane of ferroelectric $BaTiO_3$.[15] Our first-principles calculations based on density functional theory (DFT) predict that a point Vo produces a 0D defect-dipole complex in the spontaneous polar phase of $BaTiO_3$ under the square-tensile-strain (see Figure 1b and the Materials and Methods in the Supporting Information). Figure 1b illustrates the theoretical results of local $Ti^{3+}$ and $O^{2-}$ ion displacements when a $V_O$ is located at a vertex of two corner-sharing $TiO_6$ octahedra along the [010]-axis and the $P_{FE}$ is oriented along the [100]-direction in square-tensile-strained (001) plane of $BaTiO_3$. We find that the canted displacement of $Ti^{3+}$ ions for a $V_O$ at a vertex of the [010]-axis produces a finite $P_d$ along the opposite

F. U. H. Naqvi, J.-H. Ko
School of Nano Convergence Technology
Nano Convergence Technology Center
Hallym University
Chuncheon 24252, Republic of Korea
J.-S. Bae
Busan Center
Korea Basic Science Institute (KBSI)
Busan 46742, Republic of Korea
J. Kim
Department of Physics
Pohang University of Science and Technology (POSTECH)
Pohang, Gyeongbuk 790-784, Republic of Korea
T. K. Song
Department of Materials Convergence and System Engineering
Changwon National University
Changwon, Gyeongnam 51140, Republic of Korea
H. Y. Jeong
UNIST Central Research Facilities
Ulsan National Institute of Science and Technology
Ulsan 44919, Republic of Korea

 

direction of $P_{FE}$//[100], exhibiting the lowest total energy of the system (Figure 1b and Figure S2e, Supporting Information). Thus, the canted $Ti^{3+}$–$V_O$–$Ti^{3+}$ complex, consisting of two $Ti^{3+}$ ions and a $V_O$, builds up $P_d$ in the opposite direction of $P_{FE}$, where the $P_d$ can act as a source of a local internal field in polarization reversal microscopically. For the as-grown pristine state, $P_{FE}$ could develop 90° domain walls with four polarization variants in the square strained (001) plane to minimize electrostatic energy[15,16] and induce an energetically favored antiparallel $P_d$ to the $P_{FE}$ (Figure 1a). The 90° domains and antiparallel $P_d$-$P_{FE}$ arrangement would result in the pinched hysteresis loop for the pristine state.[14] On the other hand, external application of the electric field under sufficiently high thermal energy for the $V_O$ to migrate in the lattice[17] could induce a single domain and manipulate the direction of the $P_d$, characterized by biased ferroelectric hysteresis loop with the orientational dependent $E_{bias}$. We successfully demonstrate deterministic control of the $E_{bias}$ in $P(E)$, and thereby, ternary in-plane polar configurations are achievable in the remanent state at room temperature.

## 2. Results and Discussion

In order to induce square-tensile-strain to the $BaTiO_3$ film, we develop a new substrate of cubic perovskite oxide $BaZrO_3$ with a large lattice constant of 4.189 Å (see **Figure 2**a and Figure S3 and the Materials and Methods in the Supporting Information). The $BaTiO_3$ epitaxy films on the $BaZrO_3$ substrates are grown on the (001) surface by pulsed laser deposition (PLD) (see the Materials and Methods in the Supporting Information). Annular dark-field (ADF) scanning transmission electron microscopy (STEM) images (Figure 2b) represent that the $BaTiO_3$ film is epitaxially grown on the $BaZrO_3$ substrate. The reciprocal space maps (RSMs) of {204} Bragg reflections of the $BaTiO_3$ film (Figure 2c and Figure S9, Supporting Information)

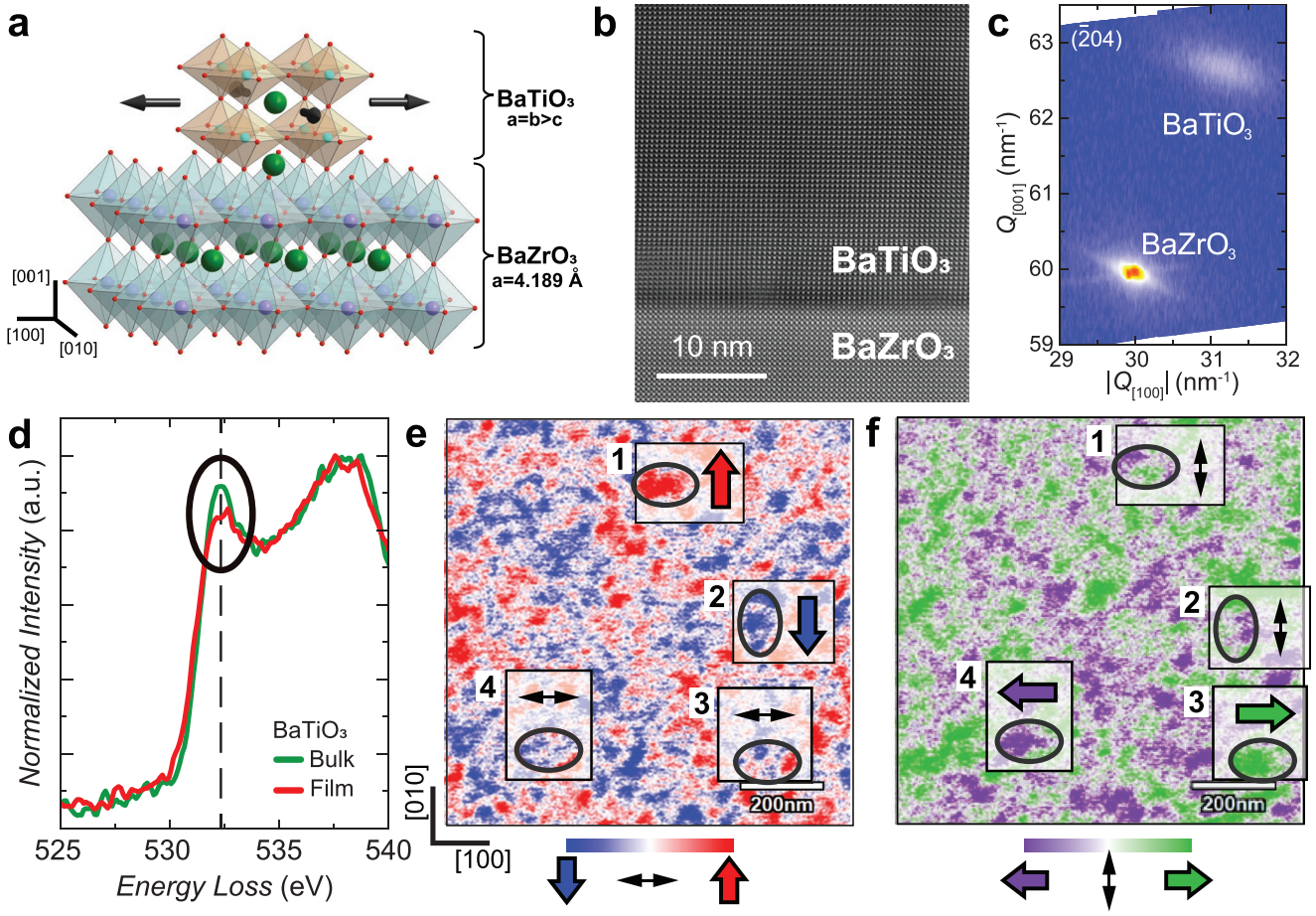


**Figure 2.** $c/a < 1$ tetragonally distorted $BaTiO_3$ film on the cubic $BaZrO_3$ substrate and four-variants in-plane polar domains. a) Schematic of a $c/a < 1$ tetragonal unit cell of square-tensile-strained $BaTiO_3$ film on the cubic perovskite $BaZrO_3$ substrate. b) Cross-sectional ADF-STEM image of the $BaTiO_3$ film and $BaZrO_3$ substrate. c) RSMs at $(\bar{2}04)$ reflections for the $BaTiO_3$ film and $BaZrO_3$ substrate. Here, the [001]-direction corresponds to out of the sample surface plane. Strong and sharp $BaZrO_3$ substrate peaks exist near $Q_{[001]} = 59.96$ nm$^{-1}$ and $|Q_{[100]}| = 29.98$ nm$^{-1}$, and weak $BaTiO_3$ film peaks are observed near $Q_{[001]} = 62.68$ nm$^{-1}$ and $|Q_{[100]}| = 31.11$ nm$^{-1}$, which indicate $c = 4.009(7)$ Å and $a = b = 4.039(3)$ Å, respectively. d) EELS results of the O *K*-edge taken from the 66 nm thick $BaTiO_3$ film (red) and the $BaTiO_3$ bulk single crystal (green). The EELS spectra of the $BaTiO_3$ film show a decreased near-edge fine-structure at 532.3 eV, which indicates the existence of oxygen vacancies $V_O$s in the $BaTiO_3$ film. The dashed line guides the normalized intensity at energy losses of 532.3 eV. e,f) IP-PFM image simultaneously taken by a tip of which the cantilever axis orients along the [100]-direction (e) and the [010]-direction (f). The colored solid arrows imply the direction of the in-plane polarization.

determine that the out-of-plane $c$//[001], in-plane $a$//[100], and $b$//[010] lattice constants of the $BaTiO_3$ film are $c = 4.009(7)$ Å and $a = b = 4.039(3)$ Å, respectively. The azimuthal angle ($\phi$)-independent $|Q_x|$(or $|Q_y|$) and $Q_z$ values for the {204} reflections of the $BaTiO_3$ film indicate that the lattice of the $BaTiO_3$ film maintains fourfold symmetry in the (001) plane (see the Materials and Methods in the Supporting Information). In addition, Raman spectra of the $BaTiO_3$ film (Figure S10, Supporting Information) clearly show two predominant peaks at 301 and 526 $cm^{-1}$ correspond to representative Raman spectra of the tetragonal $BaTiO_3$ bulk single crystal.[18] Thus, both experiments indicate that the in-plane square tensile stress of the $BaZrO_3$ substrate leads to a $c/a = 0.99 < 1$ tetragonal lattice distortion of the epitaxial $BaTiO_3$ film rather than an orthorhombic[19] or a monoclinic[20] distortion, at least in these measurements scale. In the electron energy-loss spectroscopy (EELS) spectra (Figure 2d) and X-ray photoelectron spectroscopy spectra (Figure S11, Supporting Information), we observe the decreased near-edge fine structure (Figure 2d) and the increased $V_O$ peaks (Figure S11, Supporting Information) of the $BaTiO_3$ film in comparison with that of the bulk $BaTiO_3$ single crystal. It reveals that the $BaTiO_3$ film incorporates more $V_O$s than the bulk $BaTiO_3$ single crystal.

The ab-initio-based molecular dynamic simulations in a box of $32 \times 32 \times 32$ unit cells expected that the square-tensile-strain on $BaTiO_3$ stabilizes a multidomain ferroelectric phase with electric polarization along ⟨100⟩, in which the elastic boundary condition through the epitaxial constraint of the square-tensile-strain favors the tetragonal phase.[15] We performed in-plane piezoresponse force microscopy (IP-PFM) measurements of a pristine $BaTiO_3$ film (see Figure 2e,f, and Figure S14 and the Materials and Methods in the Supporting Information), which reveal four-variants polar domains with irregular distribution and meandering boundaries in nanoscale. For the archetypal ferroelectric domain structures of $BaTiO_3$, the crystallographic symmetry and saved electrostatic energy at the domain walls favor the stripe patterns of 90° domain walls.[15,16] On the other hand, in epitaxial ferroelectric films, the substrate surface symmetry constrains elastic variants and strongly affects the domain structures. For example, four in-plane ferroelectric variants of $BiFeO_3$ films are constrained on $SrTiO_3$ (110) substrates.[21] In the epitaxial $BaTiO_3$ film on the $BaZrO_3$ substrates, spontaneous in-plane polarization breaks the fourfold symmetry in the *ab*-plane and should allow orthorhombic twofold symmetry. Nevertheless, the fourfold symmetric square lattice of the $BaZrO_3$ (001) surface could compel the four-variants in-plane polar domains. In the macroscopic scale, the averaged structural symmetry of the orthorhombic nanodomains with four-variants would appear to be fourfold tetragonal, which is in agreement with our results observed in the X-ray diffraction (XRD) and Raman analyses. From this experimental evidence of a $c/a < 1$ tetragonal lattice distortion (characterized by macroscopic XRD and Raman measurements) and four-variants polar domains (microscopically observed in the IP-PFM measurements), we conclude that the square tensile stress of the $BaZrO_3$ substrate produces a tetragonally distorted $BaTiO_3$ film with four-variants orthorhombic (*Pmm*2) nanodomains, where spontaneous polarization breaks the fourfold symmetry in the *ab*-plane of $a = b > c$.

**Figure 3**a–c represents experimental results of $P(E)$ measurements of a $BaTiO_3$ film with the interdigital electrodes along the [100]- and [110]-directions (see the inset of Figure S16a and the Materials and Methods in the Supporting Information). The pristine state of the $BaTiO_3$ film shows pinched $P(E)$, where the saturated electric polarizations $P_s$ are $P_{s,[100]} = 11.5$ μC $cm^{-2}$ for [100] and $P_{s,[110]} = 10.2$ μC $cm^{-2}$ for [110], as observed in the aged ferroelectrics. Under sufficiently high thermal energy for $V_O$ to migrate in the lattice, the $P_d$ is oriented along with directions of the applied electric field or the $P_{FE}$.[17] We designed a poling process[5] to align and switch the $P_d$ direction in a square-tensile-strained $BaTiO_3$ film (Figure S15a, Supporting Information). The specimen was cooled down under a constant applied electric field $E_{pole}$ along the [100]- or [110]-direction from $T = 120$ °C, and then, after $E_{pole}$ was turned off at room temperature ($T = 27$ °C), $P(E)$ was measured. The positively poled state reveals distinct negative-biased ferroelectric $P(E)$ (Figure 3b) with bias-fields $E_{bias,[100]} = -33.3$ kV $cm^{-1}$ for [100] and $E_{bias,[110]} = -43.3$ kV $cm^{-1}$ for [110], where the anisotropy of $P_s$ ($P_{s,[100]} = 12.9$ μC $cm^{-2}$ and $P_{s,[110]} = 9.1$ μC $cm^{-2}$) increases to $P_{s,[100]}/P_{s,[110]} \approx \sqrt{2}$. Negative poling switches to positive-biased ferroelectric $P(E)$ while maintaining the anisotropy and magnitude of $P_s$ (Figure 3c). The $E_{bias}$ is reversibly manipulated by thermal treatment and the subsequent electrical poling. In addition, zero-field cooling (ZFC) restores the pinched $P(E)$ and preserves the anisotropic $P_s$ (Figure S16, Supporting Information). Thus, three types of in-plane polar states with distinct $P(E)$ are reproducibly controlled by the electric field cooling process (sMaterials and Methods in the Supporting Information).

In addition, the $E_{bias}$ in the $P(E)$ measurements corresponds to an internally induced electric field by the $P_d$. Contrary to the imprint due to the spatial potential gradients,[5,7] the $E_{bias,[110]}$ and $E_{bias,[100]}$ of the $BaTiO_3$ film exhibit the apparent anisotropy of $E_{bias,[110]}/E_{bias,[100]} = 1.3–\sqrt{2}$ (Figure 3b,c). A combination of $V_O$ existence and anisotropic $E_{bias}$ provides evidence that the $E_{bias}$ of the $BaTiO_3$ film originates from an orientational-dependent $P_d$ of the $Ti^{3+}$–$V_O$–$Ti^{3+}$ complex in the lattice. Epitaxial strain, lattice expansion, the energetics of the PLD growth, and non-stoichiometry related effects could yield cations ($Ba^{2+}$, $Ti^{4+}$) and oxygen vacancies, which form the $P_d$ for the complex oxide thin films.[6,22,23] Rather than other vacancies of the cations, the $V_O$ requires the order of magnitude lower thermodynamic energy to get mobility.[22] The poling temperature of $T = 120$ °C for the $P_d$ is within that of the $V_O$ for our poling process.[22] Therefore, the $P_d$ associated with switchable $E_{bias}$ for the three types of polar states is attributed to the $V_O$ rather than the cation vacancies.

Adopting the canted $Ti^{3+}$–$V_O$–$Ti^{3+}$ complex model for $P_d$, we illustrate how $P_{FE}$, $P_d$, and $V_O$ cooperate in the $P(E)$ measurements (Figure 3, right). At $E = 0$ kV $cm^{-1}$ of the pristine state (Figure 3a and Figure S16a, Supporting Information), $P_{FE}$ develops 90° domain walls to minimize electrostatic energy[15,16] at the domain wall parallel to the (110) plane and induces the energetically favored antiparallel $P_d$ to the $P_{FE}$ based on the DFT calculations. Applying external $E$ to the pristine aligns the $P_{FE}$ to the direction of the $E$ but not the $P_d$ because of insufficient thermal energy at room temperature.[17] The $P_d$ plays a role in restoring force to reverse $P_{FE}$ and results in pinched $P(E)$.[14] Increasing the temperature reduces the energy barrier

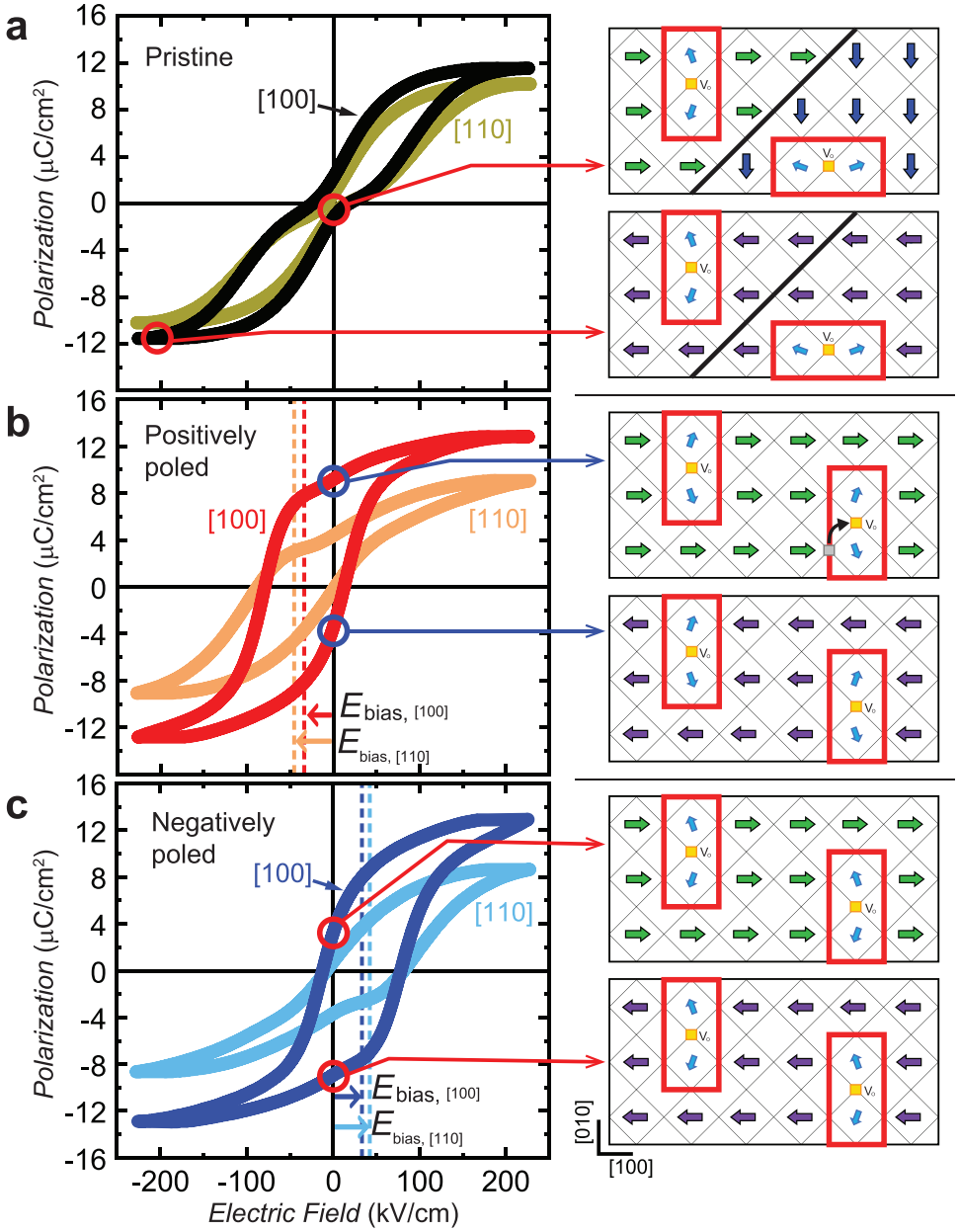


**Figure 3.** Three types of in-plane polar states and switchable ferroelectric bias. a–c) $P(E)$ hysteresis loop (left) and schematic polar domains (right) of the pristine (a), positively poled (b), and negatively poled (c) $BaTiO_3$ film. The $P(E)$ hysteresis loops were measured along the [100]- and [110]-directions at $T = 27$ °C. In the schematic of the polar domain, the colored solid arrows depict the $P_{FE}$, and the red rectangles are $Ti^{3+}$–$V_O$–$Ti^{3+}$ complex of a defect-dipole. a) The pristine $BaTiO_3$ film favors the head-to-tail 90° domain wall of the $P_{FE}$ parallel to the {110} plane for saving electrostatic energy. The finite $P_d$s are aligned opposite to $P_{FE}$ at $E = 0$ kV cm$^{-1}$ of the pristine state. b,c) Poling-dependent bias-field in the ferroelectric $P(E)$ along the [100] (dark colors) and [110] (light colors) directions. The positive and negative polings produce negatively and positively biased ferroelectric $P(E)$, respectively, where the bias-fields $E_{bias,[100]} = \mp 33.3$ kV cm$^{-1}$ along the [100] and $E_{bias,[110]} = \mp 43.3$ kV cm$^{-1}$ along the [110]. The positive poling along the [100]-direction at high temperature aligns both $P_d$ and $P_{FE}$ along the [100]-direction even through $V_O$ hopping, in which the $V_O$ at a vertex of the [100]-direction migrates to the neighboring vertex of the [010]-direction for aligning $P_d$ parallel to the poling voltage along the [100]-direction. The black arrow represents $V_O$ hopping.

for $V_O$ migration.[24] At the high temperature, application of the $E_{pole}$ along the [100]-direction aligns both $P_{FE}$ and $P_d$ in parallel along the applied $E_{pole}$ direction, in which $V_O$ of the [100]-axis migrates to the nearest vertex of the [010]-axis (Figure 3b, right). So, the poling process leads to a single domain of both $P_{FE}$ and $P_d$ along the [100]-direction. At room temperature, the applied $E$ in the $P(E)$ measurements becomes, albeit sufficiently large for switching $P_{FE}$, insufficient to switch $P_d$. Thus, $P_d$ returns to a role in the imprinted internal electric field (Figure 3b). As a result, the ferroelectric $P(E)$ of the positively (negatively) poled state is negatively (positively) biased.

An exclusive feature of the ferroelectric switchable bias, including the three types of in-plane polar states, reflects that the application of the external electric field and the prepoling

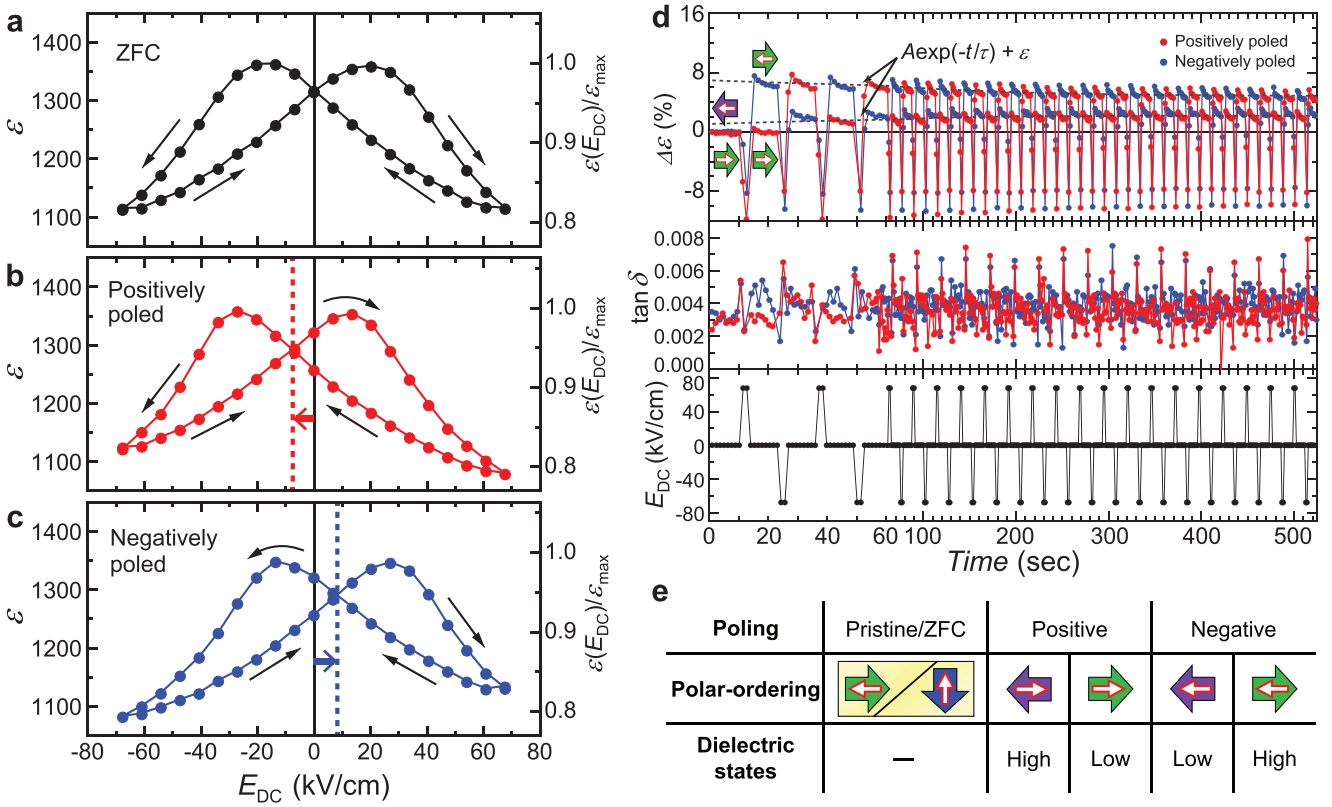


**Figure 4.** Switchable dielectric memory effect. a–c) DC electric field $E_{DC}$ dependent dielectric constant $\varepsilon$ (left axes) and $\varepsilon(E_{DC})/\varepsilon_{max}$ (right axes) along the [100]-direction for the ZFC (a), the positively poled (b), and the negatively poled (c) states, at $T = 27$ °C and with the frequency of 20 kHz. Here, the $\varepsilon_{max}$ is a maximum value of the dielectric constant of the ZFC state. d) Successive 20 cycles' switching of $\varepsilon(E_{DC} = 0)$ and loss $\tan\delta$ by applying electric field pulses of $E_{DC} = \pm 68$ kV cm$^{-1}$ to the positively (red) and the negatively (blue) poled states. The gray, open-red, and open-blue arrows depict $P_{FE}$, positively poled $P_d$, and negatively poled $P_d$, respectively. The antiparallel and parallel polar-ordering between $P_{FE}$ and $P_d$ give rise to high and low dielectric states, respectively. As the switchings are repeated, the discrepancy between dielectric constants $\Delta\varepsilon(E_{DC} = 0)$ of the high and low dielectric states is relaxed and reaches $\Delta\varepsilon \approx 30$ (2.3%), which is estimated by a relaxation function of $A\exp(-t/\tau) + \varepsilon$. $A$, $\tau$, and $\varepsilon$ for the high(low) dielectric state are $A \approx 25$ (–12), $\tau \approx 198$ (83) s, and $\varepsilon \approx 1330$ (1300), respectively. Time dependence of applied $E_{DC}$ for the successive switching experiment of $\varepsilon(E_{DC} = 0)$ in (d). The $E_{DC}$ was turned on for 2 s and off for 10 s. e) Three types of in-plane polar states of $BaTiO_3$ film on $BaZrO_3$ substrate and switchable high/low dielectric states of the in-plane polar states.

systematically controls each $P_{FE}$ and $P_d$, and determines the anisotropic interactions between $P_{FE}$ and $P_d$, similar to the switchable exchange bias effect in magnetic heterostructures.[2] We also expect that the cooperation of $P_{FE}$ and $P_d$ gives rise to distinct dielectric responses with respect to the external electric field. **Figure 4**a–c represents DC electric field $E_{DC}$ dependence of the dielectric constant $\varepsilon(E_{DC})$ for the ZFC, positively poled, and negatively poled states, respectively (Figure S16, Supporting Information). For the ZFC state, $\varepsilon(E_{DC})$ shows an archetypal symmetric butterfly shape (Figure 4a). On the other hand, the positively (Figure 4b) and the negatively (Figure 4c) poled states exhibit biased $\varepsilon(E_{DC})$, which results in discrepant values of $\varepsilon(E_{DC} = 0) = 1258$ and 1324 at the zero $E_{DC}$. Our schematic picture of $P_{FE}$ and $P_d$ domains reveals that high and low values of $\varepsilon(E_{DC} = 0)$ are determined by antiparallel and parallel alignments between $P_{FE}$ and $P_d$, respectively. Remarkably, as shown in Figure 4d, the high and low dielectric states of $\Delta\varepsilon \approx 6.5\%$ in the initial switching are alternatively reproducible with successive bipolar pulses of $E_{DC}$ for the positively and the negatively poled states. The repeated switching between the two dielectric states accompanies dielectric relaxation as a function of $A\exp(-t/\tau) + \varepsilon$, where $A$, $\tau$, and $\varepsilon$ for the high(low) dielectric state are $A \approx 25$ (–12), $\tau \approx 198$ (83) s, and $\varepsilon \approx 1330$ (1300), respectively, and reaches $\Delta\varepsilon \approx 2.3\%$. The ZFC state recovers the unpoled/zero-biased state of $\varepsilon(E_{DC} = 0) = 1316$. This demonstrates that the electrically controlled antiparallel/parallel arrangements of $P_{FE}$ and $P_d$ realize nonvolatile $\varepsilon(E_{DC} = 0)$ states (Figure 4e).

## 3. Conclusion

This study demonstrates the switchable ferroelectric bias and ternary polar states by promoting deterministic control of defect-dipole and four-variants orthorhombic (*Pmm*2) nanodomains, beyond the binary polar states.[4–7,25] We have developed a new cubic perovskite oxide substrate, $BaZrO_3$, in which large lattice constant of 4.19 Å and the cubic symmetry enable the application of extraordinarily large square tensile strain to $BaTiO_3$. The fourfold symmetric square lattice and strain on the (001) surface of the cubic perovskite $BaZrO_3$ substrate produce four variants of ⟨100⟩ in-plane electric polarization and

the domain structures. The large tensile strain also induces built-in oxygen vacancies and defect-dipoles due to the unit cell expansion. As the strain-driven built-in defect-dipole cooperates with the four-variant domains of the in-plane polarization, we have found that the electrical poling process reversibly control the orientation of the built-in defect-dipoles and the ternary polar states, characterized by the biased/pinched hysteresis loops. The development of four-variants polar domains of the $BaTiO_3$ on the $BaZrO_3$ substrate presents that the large isotropic surface lattice can spawn a novel ground state and physical phenomena in other inaccessible heterostructures, such as 2D topological phases of honeycomb superlattices on sixfold symmetric (111) surface.[26] The $BaZrO_3$ substrate will be harnessed as a new platform for artificial design to a conceptual material system via heteroepitaxy inevitably combined with strain engineering. In addition, the switchable dielectric states inspire that the dielectric constant, rather than the electrical resistivity, can be considered a low-energy-consumption memory information.

## 4. Experimental Section

*$BaZrO_3$ Single-Crystal Growth, Substrate Preparations, and Physical Properties*: $BaZrO_3$ is one of a few cubic perovskite oxides and has a large lattice constant of 4.189 Å (Figure S3a, Supporting Information). The high melting temperature $T = 2690$ °C[27] of $BaZrO_3$ and severe evaporation of BaO inhibit single-crystal growth under ordinary substrate growth environments, and high-quality growth can be achieved using the optical floating zone method[28] and the induction skull melting method.[29] A 4 cm long $BaZrO_3$ single crystal of ≈4 mm diameter (Figure S3b, Supporting Information) was successfully grown by optimizing the growth condition of the reported optical floating zone method.[28] Polycrystalline $BaZrO_3$ feed rods were prepared as stoichiometric BaO and $ZrO_2$ were mixed, ground, pelletized, and sintered at 1650 °C for 24 h in air. $BaZrO_3$ single crystals were grown using the optical floating zone (FZ-T-12000-X-VII-VPO-PC, Crystal System) in a 10% $O_2$ and 90% Ar mixed gas environment under a pressure of 5 bar and flow rate of 4 L $min^{-1}$. Anticlockwise rotation of the feed and seed rods at 20 rpm was carried out. The travelling speeds, optimized to maintain the stable molten zone, were 12.9 and 9.2 mm $h^{-1}$ for the feed and seed rods, respectively. The as-grown single crystals were annealed at 1650 °C in $O_2$ flow. The grown $BaZrO_3$ single-crystal rod had a diameter of 4–5 mm and length of ≈4 cm as shown in Figure S3b in the Supporting Information. The sliced $BaZrO_3$ single-crystal disks were polished using an Allied High Tech Multiprep Polishing System and a Pace Technologies GIGA-1200 Vibratory Polisher.

The cylindrical axis of the grown $BaZrO_3$ single crystal tends oriented along the crystallographic [001] axis (Figure S3c, Supporting Information). Once the (001) cleaved surface was achieved by cleaving perpendicular to the cylindrical axis, the (001) $BaZrO_3$ substrate was prepared by slicing or cleaving another (001) surface and polishing both surfaces (Figure S3d, Supporting Information). The root-mean-square (RMS) surface roughness of the polished (001) surface was as low as 1.58 Å (Figure S3e, Supporting Information). The full-width half-maximum (FWHM) from the rocking curve (Figure S3f, Supporting Information) was 0.021°–0.075°, comparable to that of the prevalent $SrTiO_3$ substrates. $BaZrO_3$ is an ultrawide bandgap semiconductor;[30] hence, optical transmittance spectra (Figure S3g, Supporting Information) and Tauc plots (Figure S3h,i, Supporting Information) exhibited direct 4.97 eV and indirect 4.88 eV energy bandgaps. The near-edge defect state, resolved from the Urbach tail in Tauc plots, was negligible in comparison with both the reported and commercial single crystals.[28] The dielectric constant $\varepsilon$ and loss $\tan\delta$ at $f = 20$ kHz along the [001] axis were ≈55 and ≈0.001, respectively, at room temperature (Figure S3j, Supporting Information). As the temperature decreased, $\varepsilon$ gradually increased and a weak dielectric anomaly appeared at $T = 150$ K with a peak of $\tan\delta$ as observed in previous reports.[31,32] These studies attributed such dielectric anomaly to several reasons, e.g., polaronic relaxation,[33] unavoidable impurities,[31] and dynamic Jahn–Teller-like octahedra distortion.[34] Still, the origin of this anomaly was unclear and required further comprehensive investigation. $BaZrO_3$ was consisted of only diamagnetic, so-called nonmagnetic, $Ba^{2+}$, $Zr^{4+}$, and $O^{2-}$ ions; thus, the magnetic susceptibility was negative, $\chi_{dc} \approx -55 \times 10^{-6}$ emu $mole^{-1}$, and nearly temperature independent.

*Film Growth*: $BaTiO_3$ films were epitaxially fabricated on $BaZrO_3$ (001) substrates using the PLD method. The film thickness of all $BaTiO_3$ films was 60–70 nm. The epitaxy and the thickness of the as-grown $BaTiO_3$ (001) films were characterized by a lab-based X-ray diffractometer (D8 Advance, Bruker). A pulsed excimer laser (KrF, wavelength of 248 nm) was irradiated into a $BaTiO_3$ ceramic target to generate a plasma plume for film growth. The laser fluence for the PLD growth was about 1.1 J $cm^{-2}$. Before the actual film deposition, the surface of the ceramic target was preablated with a pulsed laser for a particular duration. $BaTiO_3$ films were deposited at 650 °C under an oxygen partial pressure of 20 mTorr. Subsequently, in situ post-annealing was performed at 630 °C for 1 h under the oxygen environment of 100 Torr. In addition, all $BaTiO_3$ films were ex situ annealed at 600 °C for 3 h in an oxygen atmosphere under the ambient pressure in the tube furnace. The specimen's state after the film growth and the ex situ annealing was called pristine state.

*Crystallographic Structure of $BaTiO_3$ Film on the $BaZrO_3$ Substrate*: The FWHM in (002) rocking curves of the ex situ annealed $BaTiO_3$ films (Figure S4, Supporting Information) was 0.15°–0.40°. ADF-STEM, the temperature dependence of XRD, EELS, $P(E)$, and electro-dielectric memory effect were examined on film-a. Contact resonance of the PFM was measured on film-b. XRD, RSM, Raman scattering, and IP-PFM were performed on film-c. The 66 nm film thickness of film-a was verified by the cross-sectional ADF-STEM images (Figure S5a, Supporting Information). Even though the large lattice mismatch of 4.49% between $BaTiO_3$ and $BaZrO_3$ led to the edge dislocation at the interface between the $BaTiO_3$ film and the $BaZrO_3$ substrate (Figure S5b, Supporting Information), the epitaxial $BaTiO_3$ (001) films were successfully grown, in which FWHM was 0.15°–0.40°. Due to the large nominal misfit strain of 4.49% between $BaTiO_3$ and $BaZrO_3$, the $BaTiO_3$ lattice constants were observed to rapidly relax, when the $BaTiO_3$ film layer was away from the $BaTiO_3/BaZrO_3$ interface (Figure S6, Supporting Information).

$\theta$–$2\theta$ XRD showed clear (00$l$) Bragg reflections of the $BaTiO_3$ film and $BaZrO_3$ substrate (Figure S7, Supporting Information). A $\phi$-scan of {101} Bragg peaks of the $BaTiO_3$ film and $BaZrO_3$ substrate (Figure S8, Supporting Information) presented that the $BaTiO_3$ film was epitaxially grown on the $BaZrO_3$ substrate. From the RSMs of {204} Bragg reflections of the $BaTiO_3$ film (Figure S9, Supporting Information), it was determined that the out-of-plane $c$, in-plane $a$, and $b$ lattice constants of the $BaTiO_3$ film were $c = 4.009(7)$ Å and $a = b = 4.039(3)$ Å, respectively. A tensile strain $\eta = +0.98\%$ ($\eta = 100 \times (a/a_{pc,0} - 1)$, where $a_{pc,0}$ is the cube root of volume of bulk tetragonal $BaTiO_3$ at $T = 20$ °C; $a_{pc,0} = 4.000(4)$ Å[35]) was applied to the 66 nm thick $BaTiO_3$ film.

Raman spectra of the $BaTiO_3$ film (Figure S10, Supporting Information) clearly showed two predominant peaks at 301 and 526 $cm^{-1}$ corresponded to representative Raman spectra of the tetragonal $BaTiO_3$ bulk single crystal.[18] Thus, both experiments indicated that the square tensile stress of the $BaZrO_3$ substrate led to a $c/a = 0.99 < 1$ tetragonal lattice distortion of the epitaxial $BaTiO_3$ film rather than an orthorhombic[19] or a monoclinic[20] distortion, at least in these measurements scale.

The change in slope of the temperature dependence of the lattice constant had often been referred to as evidence of a ferroelectric phase transition.[19,36] The temperature dependence of the in-plane lattice constant of the square-tensile-strained $BaTiO_3$ film on the $BaZrO_3$ substrate exhibited a change in slope at ≈415 °C (Figure S12, Supporting Information), close to the predicted $T_c$ from ab initio calculations[15] and higher than that on $MgAl_2O_4$ substrate.[19]

*PFM Measurements*: The space group *Pmm*2 has 2mm symmetry, where the twofold axis is parallel to the polar [100] axis. The symmetry allowed the following piezoelectric tensor

$$d_{ij} = \begin{pmatrix} d_{11} & d_{12} & d_{13} & 0 & 0 & 0 \\ 0 & 0 & 0 & 0 & 0 & d_{26} \\ 0 & 0 & 0 & 0 & d_{25} & 0 \end{pmatrix} \quad (1)$$

where index $i$, $j$ = 1, 2, 3 correspond to [100], [010], [001] axes. The conventional geometry of the IP-PFM measurement probed the shear piezoelectric response $d_{25}$ of the *Pmm*2 orthorhombic $BaTiO_3$ film.

IP-PFM measurement was conducted over an area of 1 µm × 1 µm with a condition of 256 lines using a commercial scanning probe microscope (Asylum Research MFP 3D Infinity, Oxford Instruments). Conductive Pt-coated silicon tips (MikroMasch, HQ:NSC35/Pt) were used. Tip scanning speed was 2 µm $s^{-1}$ and an AC voltage of 3 V was applied to the tip during PFM scans. The longest cantilever tip with 130 µm was selected to avoid large loading forces imposed on the sample. To enhance the signal, PFM images were measured in near resonance conditions at 1.29 MHz. The reproducibility of the IP-PFM images was verified by correcting the signal offset and taking several consecutive measurements on the same area.

Contact resonance of the PFM in Figure S13 in the Supporting Information was performed by an atomic force microscope (NX10, Park Systems) with a lock-in amplifier (HF2LI, Zurich Instruments). IP-PFM measurements were performed through the lateral oscillation of a nonconductive cantilever while an AC voltage $V_{ac}$ of ±5 V was applied to a pair of interdigital electrodes along the [110] or [100] directions.[37] To obtain a high signal-to-noise ratio, dual-amplitude-resonance-tracking PFM mode was used. Note that the $BaTiO_3$ film had no bottom electrodes and nonconductive cantilevers (PPP-FMR, Nanosensors) were used. The applied $V_{ac}$ of 5 V between 5 µm gaps of the interdigital electrode's fingers was corresponded to the electric field of 10 kV $cm^{-1}$, 22% of the coercive field in the $P(E)$ of the electrically poled state. The first harmonic contact resonance frequency of the IP-PFM signals was ≈770 kHz (Figure S13, Supporting Information). The in-plane piezoresponse, measured by the PFM, was a factor of ten larger than the out-of-plane piezoresponse (Figure S13, Supporting Information). These results indicated that the predominant piezoresponse of epitaxial $BaTiO_3$ film on the $BaZrO_3$ substrate arose from in-plane components of the film rather than out-of-plane direction (the [001] direction).

## Supporting Information

Supporting Information is available from the Wiley Online Library or from the author.

## Acknowledgements

C. B. Eom and S.-W. Cheong are thanked for constructive comments on the manuscript. This work was supported by the Basic Science Research Programs through the National Research Foundation of Korea (NRF) (NRF-2020R1A2C1009537). N.X.D., C.W.A., and T.H.K. acknowledge support from the Priority Research Centers Program through the National Research Foundation of Korea (NRF) funded by the Ministry of Education (NRF-2019R1A6A1A11053838) and support by the National Research Foundation of Korea (NRF) grants funded by the Ministry of Science and ICT (NRF-2022R1A2C1006389). H.Y.J. acknowledges support from the Creative Materials Discovery Program through the National Research Foundation of Korea (NRF-2016M3D1A1900035). K.P. acknowledges support by the National Research Foundation of Korea (NRF) grants funded by the Ministry of Science and ICT (NRF-2020M3F3A2A02082437). C.-H.Y. acknowledges support by the National Research Foundation of Korea (NRF) grants funded by the Korean Government through the Creative Research Center for Lattice Defectronics (2017R1A3B1023686). Experiments at the PLS-II 3A beamline were supported in part by the Ministry of Science and ICT (MSIT) of the Korean government. Initial preliminary work on polishing substrate by Y.S.O. at Rutgers was supported by the visitor program at the center for Quantum Materials Synthesis (cQMS), funded by the Gordon and Betty Moore Foundation's EPiQS initiative through grant GBMF10104, and by Rutgers University.

## Conflict of Interest

The authors declare no conflict of interest.

## Data Availability Statement

The data that support the findings of this study are available from the corresponding author upon reasonable request.

## Keywords

$BaZrO_3$, defect-dipoles, ferroelectrics, four-variants ferroelectric domains, in-plane ferroelectrics, new perovskite substrates, switchable ferroelectric bias, ternary polar states

Received: June 27, 2022
Revised: August 17, 2022
Published online:

[1] W. H. Meiklejohn, C. P. Bean, *Phys. Rev.* **1957**, *105*, 904.
[2] J. Nogués, I. K. Schuller, *J. Magn. Magn. Mater.* **1999**, *192*, 203.
[3] a) I. Dzyaloshinsky, *J. Phys. Chem. Solids* **1958**, *4*, 241; b) T. Moriya, *Phys. Rev.* **1960**, *120*, 91; c) S. W. Cheong, M. Mostovoy, *Nat. Mater.* **2007**, *6*, 13.
[4] G. Arlt, H. Neumann, *Ferroelectrics* **1988**, *87*, 109.
[5] W. L. Warren, D. Dimos, G. E. Pike, B. A. Tuttle, M. V. Raymond, R. Ramesh, J. T. Evans, *Appl. Phys. Lett.* **1995**, *67*, 866.
[6] A. R. Damodaran, S. Pandya, Y. Qi, S. L. Hsu, S. Liu, C. Nelson, A. Dasgupta, P. Ercius, C. Ophus, L. R. Dedon, J. C. Agar, H. Lu, J. Zhang, A. M. Minor, A. M. Rappe, L. W. Martin, *Nat. Commun.* **2017**, *8*, 14961.
[7] P. Buragohain, A. Erickson, P. Kariuki, T. Mittmann, C. Richter, P. D. Lomenzo, H. Lu, T. Schenk, T. Mikolajick, U. Schroeder, A. Gruverman, *ACS Appl. Mater. Interfaces* **2019**, *11*, 35115.
[8] E. G. Lee, D. J. Wouters, G. Willems, H. E. Maes, *Appl. Phys. Lett.* **1996**, *69*, 1223.
[9] J. Lee, C. H. Choi, B. H. Park, T. W. Noh, J. K. Lee, *Appl. Phys. Lett.* **1998**, *72*, 3380.
[10] P. Zubko, G. Catalan, A. Buckley, P. R. Welche, J. F. Scott, *Phys. Rev. Lett.* **2007**, *99*, 167601.
[11] H. Lee, T. H. Kim, J. J. Patzner, H. Lu, J. W. Lee, H. Zhou, W. Chang, M. K. Mahanthappa, E. Y. Tsymbal, A. Gruverman, C. B. Eom, *Nano Lett.* **2016**, *16*, 2400.
[12] P. W. Blom, R. M. Wolf, J. F. Cillessen, M. P. Krijn, *Phys. Rev. Lett.* **1994**, *73*, 2107.
[13] a) J. F. Scott, *Ferroelectric Memories*, Springer, Berlin/Heidelberg, Germany **2000**; b) M. E. Lines, A. M. Glass, *Principles and Applications of Ferroelectrics and Related Materials*, Oxford University Press, Oxford, UK **2001**; c) M. Dawber, K. M. Rabe, J. F. Scott, *Rev. Mod. Phys.* **2005**, *77*, 1083.
[14] X. Ren, *Nat. Mater.* **2004**, *3*, 91.

 

[15] A. Grünebohm, M. Marathe, C. Ederer, *Appl. Phys. Lett.* **2015**, *107*, 102901.
[16] a) L. X. Zhang, X. Ren, *Phys. Rev. B* **2005**, *71*, 174108; b) P. Marton, I. Rychetsky, J. Hlinka, *Phys. Rev. B* **2010**, *81*, 144125.
[17] a) W. L. Warren, G. E. Pike, K. Vanheusden, D. Dimos, B. A. Tuttle, J. Robertson, *J. Appl. Phys.* **1996**, *79*, 9250; b) D. Lee, B. C. Jeon, S. H. Baek, S. M. Yang, Y. J. Shin, T. H. Kim, Y. S. Kim, J. G. Yoon, C. B. Eom, T. W. Noh, *Adv. Mater.* **2012**, *24*, 6490.
[18] J. D. Freire, R. S. Katiyar, *Phys. Rev. B: Condens. Matter Mater. Phys.* **1988**, *37*, 2074.
[19] K. Komatsu, I. Suzuki, T. Aoki, Y. Hamasaki, S. Yasui, M. Itoh, T. Taniyama, *Appl. Phys. Lett.* **2020**, *117*, 072902.
[20] J. W. Lee, K. Eom, T. R. Paudel, B. Wang, H. Lu, H. X. Huyan, S. Lindemann, S. Ryu, H. Lee, T. H. Kim, Y. Yuan, J. A. Zorn, S. Lei, W. P. Gao, T. Tybell, V. Gopalan, X. Q. Pan, A. Gruverman, L. Q. Chen, E. Y. Tsymbal, C. B. Eom, *Nat. Commun.* **2021**, *12*, 6784.
[21] Y. H. Chu, M. P. Cruz, C. H. Yang, L. W. Martin, P. L. Yang, J. X. Zhang, K. Lee, P. Yu, L. Q. Chen, R. Ramesh, *Adv. Mater.* **2007**, *19*, 2662.
[22] P. Erhart, K. Albe, *J. Appl. Phys.* **2007**, *102*, 084111.
[23] Q. Yang, J. X. Cao, Y. Ma, Y. C. Zhou, L. M. Jiang, X. L. Zhong, *J. Appl. Phys.* **2013**, *113*, 184110.
[24] A. V. Kimmel, P. M. Weaver, M. G. Cain, P. V. Sushko, *Phys. Rev. Lett.* **2012**, *109*, 117601.
[25] Y. Kadota, H. Hosaka, T. Morita, *Ferroelectrics* **2010**, *368*, 185.
[26] D. Xiao, W. Zhu, Y. Ran, N. Nagaosa, S. Okamoto, *Nat. Commun.* **2011**, *2*, 596.
[27] R. Vassen, X. Cao, F. Tietz, D. Basu, D. Stöver, *J. Am. Ceram. Soc.* **2004**, *83*, 2023.
[28] C. Xin, P. Veber, M. Guennou, C. Toulouse, N. Valle, M. Ciomaga Hatnean, G. Balakrishnan, R. Haumont, R. Saint Martin, M. Velazquez, A. Maillard, D. Rytz, M. Josse, M. Maglione, J. Kreisel, *CrystEngComm* **2019**, *21*, 502.
[29] M. S. Paun, *Fakultät II - Mathematik und Naturwissenschaften*, Technische Universität Berlin, Berlin, Germany **2015**.
[30] J. Robertson, *J. Vac. Sci. Technol., B: Microelectron. Nanometer Struct.–Process., Meas., Phenom.* **2000**, *18*, 1785.
[31] A. R. Akbarzadeh, I. Kornev, C. Malibert, L. Bellaiche, J. M. Kiat, *Phys. Rev. B* **2005**, *72*, 205104.
[32] a) T. Maiti, R. Guo, A. S. Bhalla, *J. Am. Ceram. Soc.* **2008**, *91*, 1769; b) T. Kolodiazhnyi, P. Pulphol, W. Vittayakorn, N. Vittayakorn, *J. Eur. Ceram. Soc.* **2019**, *39*, 4144.
[33] O. Bidault, M. Maglione, M. Actis, M. Kchikech, B. Salce, *Phys. Rev. B* **1995**, *52*, 4191.
[34] C. Toulouse, D. Amoroso, C. Xin, P. Veber, M. C. Hatnean, G. Balakrishnan, M. Maglione, P. Ghosez, J. Kreisel, M. Guennou, *Phys. Rev. B* **2019**, *100*, 134102.
[35] H. D. Megaw, *Nature* **1945**, *155*, 484.
[36] K. J. Choi, M. Biegalski, Y. L. Li, A. Sharan, J. Schubert, R. Uecker, P. Reiche, Y. B. Chen, X. Q. Pan, V. Gopalan, L. Q. Chen, D. G. Schlom, C. B. Eom, *Science* **2004**, *306*, 1005.
[37] S. Y. Yang, J. Seidel, S. J. Byrnes, P. Shafer, C. H. Yang, M. D. Rossell, P. Yu, Y. H. Chu, J. F. Scott, J. W. Ager3rd, L. W. Martin, R. Ramesh, *Nat. Nanotechnol.* **2010**, *5*, 143.